Chemistry—Methods

Research Article
doi.org/10.1002/cmtd.202200015

Chemistry Europe
European Chemical Societies Publishing

www.chemistrymethods.org

Special Issue

Following Cu Microstructure Evolution in CuZnO/Al_2O_3(–Cs) Catalysts During Activation in H_2 using in situ XRD and XRD-CT

Daniela M. Farmer,[a, b] Simon D. M. Jacques,[c] David Waller,[d] Sara Boullosa Eiras,[d] Kanak Roy,[e] Georg Held,[e] Gopinathan Sankar,[a] and Andrew M. Beale*[a, b, c]

Understanding how the microstructure of the active Cu^0 component in the commercially applicable Cu/ZnO/Al_2O_3(–Cs_2O) low-temperature water-gas shift catalyst evolves under various H_2 partial pressures in the presence/absence of a Cs promoter during thermal activation has been investigated. Time-resolved XRD and spatially-resolved XRD-CT data were measured as a function of H_2 concentration along a packed bed reactor to elucidate the importance of the zincite support and the effect of the promoter on Cu sintering mechanisms, dislocation character and stacking fault probability. The rate of Cu reduction showed a dependency on [Cs], [H_2] and bed height; lower [Cs] and higher [H_2] led to a greater rate of metallic copper nanoparticle formation. A deeper analysis of the XRD line profiles allowed for determining a greater edge character to the dislocations and subsequent stacking fault probability was also observed to depend on higher [H_2], smaller Cu^0 (and ZnO) crystallite sizes, increased [ZnO] (30 wt.%, sCZA) and lower temperature. The intrinsic activity of Cu/ZnO/Al_2O_3 methanol synthesis catalysts has been intimately linked to the anisotropic behaviour of copper, and thus the presence of lattice defects; to the best knowledge of the authors, this study is the first instance in which this type of analysis has been applied to LT-WGS catalysts.

Introduction

The water-gas shift (WGS) reaction has been widely studied due to its ubiquitous use in industry; it aims to convert CO and H_2O into CO_2 and high-purity H_2 respectively [Eq. (1)].[1,2] Thermodynamically, the reaction favours low temperatures (190–230 °C) due to its exothermic nature making the efficiency and lifetime (4–8 years) of the low-temperature (LT-) WGS catalyst of great environmental and economic importance.[3,4] Commercial LT-WGS catalysts generally comprise 50–60/30–40 % copper and zinc oxide (Cu/ZnO) with the remaining balance γ-alumina.[3] The LT-WGS catalyst composition is very similar to that for methanol synthesis and, despite different conditions being employed, CH_3OH is an unwanted by-product of this reaction. To inhibit CH_3OH formation and maximise H_2 production, Cs is incorporated as an electronic and structural promoter (1–1.2 wt.%).[1,5]

$$\begin{aligned} &CO + H_2O \rightleftharpoons CO_2 + H_2 \\ &\Delta G_{298\ K} = -28.6\ kJ\ mol^{-1}, \\ &\Delta H_{298\ K} = -41.2\ kJ\ mol^{-1} \end{aligned} \quad (1)$$

It is accepted that the active sites on the LT-WGS catalyst are metallic copper nanoclusters.[6] A well-performing Cu/ZnO/Al_2O_3 (CZA) catalyst is therefore believed to require three key characteristics: copper nanoparticles (NPs) containing surface defects, multiple reactive Cu/ZnO interfaces, and a large Cu^0 surface area.[7–12] These are achieved following an activation procedure (using H_2 as the reducing gas), which is strictly

[a] Dr. D. M. Farmer, Prof. G. Sankar, Prof. A. M. Beale
Department of Chemistry
University College London
20 Gordon Street, London
WC1H 0AJ (UK)
E-mail: andrew.beale@ucl.ac.uk
[b] Dr. D. M. Farmer, Prof. A. M. Beale
Research Complex at Harwell
Rutherford Appleton Laboratory
Harwell Science and Innovation Campus
Harwell, Didcot, Oxon
OX11 0FA (UK)
[c] Dr. S. D. M. Jacques, Prof. A. M. Beale
Finden Ltd, Merchant House
5 East St Helen Street, Abingdon, Oxfordshire
OX14 5EG (UK)
[d] Dr. D. Waller, Dr. S. Boullosa Eiras
Yara International ASA
Yara Technology Centre
P.O. Box 1130
Porsgrunn 3905 (Norway)
[e] Dr. K. Roy, Dr. G. Held
Diamond Light Source
Harwell Science and Innovation Campus
Didcot, OX11 0DE (UK)

Supporting information for this article is available on the WWW under https://doi.org/10.1002/cmtd.202200015

Special Issue

Part of a Special Collection on In Situ and Operando Time-Resolved X-Ray and Neutron Diffraction Studies. Please visit chemistry-methods.org/collections to view all contributions.

specified by the catalyst manufacturers. Interestingly, the importance of the catalyst activation procedure employed and its subsequent influence on the microstructure of the resultant catalyst has, to the best knowledge of the authors, not been investigated for LT-WGS systems.

Investigating how changes to the activation procedure influence the microstructure of the active phase is thus paramount to understanding early onset deactivation mechanisms since for CZA catalysts, used in methanol synthesis, it is widely accepted that the Cu microstructure, specifically the defect density and apparent lattice strain, are directly correlated to catalytic performance.[7,10,12] This is because copper is strongly anisotropic, as determined by its Zener constant ($A_z = 3.28$).[13–16]

A detailed analysis of the XRD data is performed herein to evaluate lattice defects according to their strain fields, that is, how they affect the diffraction profile (shape and position) and includes consideration of:[17]

- Point defects (interstitials, vacancies and impurities) have short-range strain fields and their diffraction effects differ from the fundamental Bragg reflections.[17,18]
- Linear defects (edge and screw dislocations), also known as dislocations, have long-range strain fields. As a result, diffraction peaks appear broader as they cause a cluster effect around the fundamental Bragg peak.[17]
- Planar defects (grain and twin boundaries) are space independent/homogenous and cause deviations from the fundamental Bragg reflections, realised as shifts in peak position and changes in lattice parameter.[17]

However, the complex nature of defects means they are not generally confined to solely one category; stacking faults, for instance, cause peak broadening and a shift in peak position as they are both planar and surrounded by partial dislocations. Despite the multifaceted nature of defects, dislocations are always present to some extent in a material, either as the predominant complex lattice defect or as the only type of lattice defect which is evident by line broadening in the pattern.[17] Here, a standard low-temperature water-gas shift catalyst (sCZA, $CuO/ZnO/Al_2O_3$ 60/30/10) have been investigated in situ under three reducing atmospheres (1%, 2.5% and 5% H_2/Ar) to determine how this affects the microstructural properties of the Cu^0 component. These are compared with a high copper loading catalyst (hCZA, $CuO/ZnO/Al_2O_3$ 80/10/10) reduced under the more forcing 5% H_2 conditions to help elucidate the role of ZnO. As well as this, the incorporation of a caesium promoter (sCZA–Cs and hCZA–Cs), believed to inhibit methanol production during WGS activity, will also be assessed in terms of anisotropy, dislocations, and, finally, stacking fault probabilities.

Results and Discussion

As-prepared catalysts

The dependence of the $Cu/ZnO/Al_2O_3$ catalysts' activity upon the hydroxycarbonate precursor phase formed during coprecipitation is well documented.[19–21] For the industrial LT-WGS reaction, zincian malachite ($(Cu,Zn)_2CO_3(OH)_2$) precursors are preferred (Cu:Zn molar ratio close to 2:1) as a catalyst with high Cu dispersion, and thus higher activity is achieved.[22,23] The precursors of the sCZA and hCZA catalysts are shown in Figure 1. Malachite ($Cu_2CO_3(OH)_2$) has been included as a reference pattern to highlight how the (20-1)- and (21-1)-reflections shift to lower *d*-spacings (higher °2θ) as a result of Zn (a non-Jahn–Teller cation) being atomically substituted into the structure.[24,25] As expected, the hCZA catalyst has a lower [Zn], therefore its pattern is more crystalline and most similar to that of malachite. Both patterns indicate a hydrotalcite-like compound (HTLC) crystallising during the ageing process, which has been assigned as either a Cu HTLC, Zn HTLC or mixed Cu,Zn HTLC.[26–30] The crystallinity of the HTLC present in the sCZA pattern is greater, which may be due to the larger Zn/Al ratio.[31] The Cu:Zn ratios for sCZA and sCZA–Cs are 2.2:1 and 2.3:1, respectively, and for hCZA and hCZA–Cs are 8.8:1 and 8.9:1, respectively (Table SI-1 in Supporting Information).

Following calcination, the precursor phases completely decompose to form an intimate mixture of tenorite (CuO: 3.95, 3.96 and 4.30 °2θ) and zincite (ZnO: 3.56, 3.85 and 4.05 °2θ) as shown in Figure 2; the zincite crystallite size (Table 1) is so small it is barely visible in the diffraction pattern suggesting it is completely dispersed between the CuO species.[16,32,33] It should be noted that the tenorite crystallite sizes vary depending on the composition of the catalyst; a higher [ZnO] affords smaller CuO crystallites due to a greater interaction between the metal and support making them more stable to thermal sintering.[34] Cs-promotion also causes growth of the CuO crystallites as the

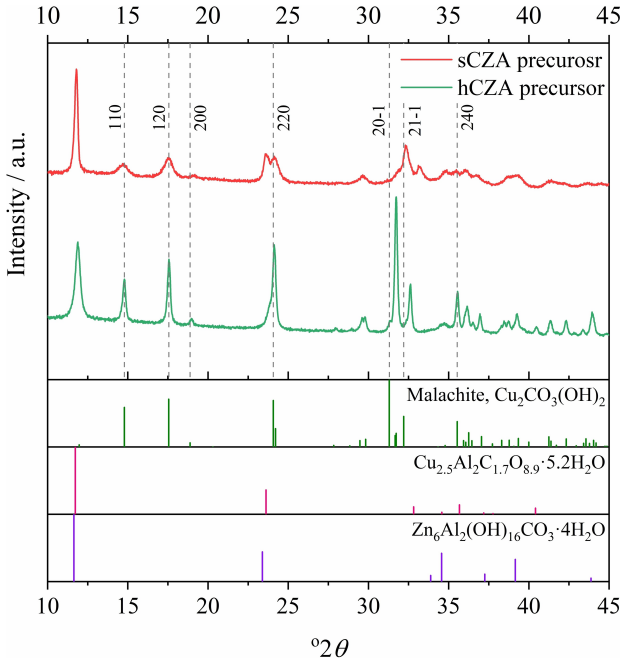

Figure 1. Diffraction patterns for the hydroxycarbonate sCZA and hCZA precursors; the dashed grey lines, from left to right, signify the (110), (120), (200), (220), (20-1), (21-1) and (240) reflections of the malachite phase, and the reference patterns for malachite ($Cu_2CO_3(OH)_2$), a Cu HTLC ($Cu_{2.5}Al_2C_{1.7}O_{8.9}\cdot 5.2H_2O$)[26] and a Zn HTLC ($Zn_6Al_2(OH)_{16}CO_3\cdot 4H_2O$)[27] are given below.

Research Article
doi.org/10.1002/cmtd.202200015
Chemistry Europe
European Chemical Societies Publishing

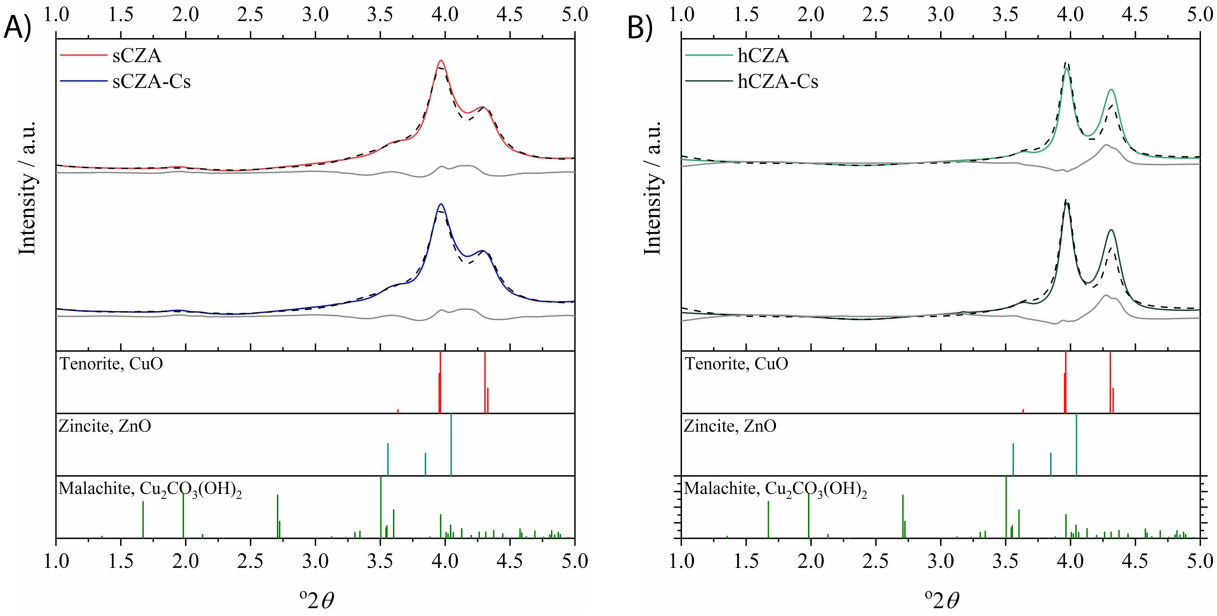

Figure 2. Diffraction patterns of the (A) sCZA, sCZA–Cs, (B) hCZA and hCZA–Cs catalysts; the calculated Rietveld fit is denoted by the dashed black line, the grey difference line, and the reference patterns for tenorite (CuO), zincite (ZnO) and malachite ($Cu_2CO_3(OH)_2$) are shown at the bottom.

Table 1. Apparent CuO and ZnO crystallite sizes for the prepared sCZA, sCZA–Cs, hCZA and hCZA-Cs catalysts.

Catalyst	Crystallite size [nm]	
	CuO	ZnO
sCZA	6.3(1)	1.0(1)
sCZA-Cs	8.0(2)	1.2(0)
hCZA	16.0(7)	1.2(0)
hCZA-Cs	16.3(8)	1.3(0)

incipient wetness impregnation method employed acts as an additional hydrothermal treatment. The larger errors associated with the high copper loading catalysts' tenorite domain sizes are anticipated to be resultant of size/strain broadening not being accounted for in the performed analysis.[35]

In situ reduction studies

Differences to the Cu^0 microstructure were determined using the Rietveld method in combination with pattern decomposition for crystal structure refinement and phase analysis. Measurements were performed at least at three different (bed) heights of the sample, delineated into (a) top, (b) middle and (c) bottom positions (as shown in Section SI-2 in Supporting Information).

Whether Cu_2O is an intermediate in the reduction of CuO in the LT-WGS catalyst is much debated in the literature.[36,37] The time-resolved point measurements collected in the middle of the (A) sCZA and (B) sCZA-Cs catalyst beds in the first 70 min of 5% H_2 being introduced (ramping in temperature from 160–230 °C) are shown in Figure 3. Following calcination, the only phases present in the diffraction patterns are CuO and ZnO. When the reducing gas is introduced, though it is not obvious, evidence of Cu_2O is most clearly seen when Cu^0 begins to show in the diffraction patterns, (see Figure 3, Cu_2O reflections denoted by the dashed orange lines). It is also confirmed in Figure 3 that the middle of the (B) Cs-promoted standard catalyst bed takes longer to reduce than that of (A) sCZA. There is no evidence of reduction of the ZnO taking place.

Crystalline phase evolution plots have been constructed for the Cu^0 component (see Figure 4 and Figures SI-3–SI-6) illustrating the reduction behaviour over time, and how this varies along the length of the catalyst bed. The time taken for Cu^0 to become the predominant phase at individual points along the catalyst beds reduced in 5%, 2.5% and 1% H_2/Ar have been plotted in Figure SI-7. The Cs-promoted catalyst appears to take longer to reduce in the higher [H_2] environment, supporting the notion that alkali metal addition inhibits reduction of the copper oxide polymorphs.[1] When the catalysts were reacted in 2.5% H_2/Ar, their reduction behaviours proved similar, (Figure SI-7 (B)). The Cs-promoted catalyst reduced slightly quicker along the length of the bed than the unpromoted form. This result more closely corresponds to the temperature-programmed reduction (TPR) results (Figure SI-8) suggesting that a higher [ZnO] has more of an affect in the presence of lower [H_2]. Complete reduction of the catalysts under 1% H_2 did not occur in the time available to perform these measurements data although the results collected are shown in Figure SI-7 (A).

The slower reduction kinetics at the top and the bottom of the bed occurred for different reasons: (1) the bottom of the reactor is cooler as the gas is at room temperature when it first contacts the bed, and (2) as water is created as a by-product of reduction, it is presumed that a high water partial pressure develops at the top of the bed which inhibits reduction. The same analysis has been applied for the high Cu loaded catalysts

Research Article
doi.org/10.1002/cmtd.202200015
Chemistry Europe
European Chemical Societies Publishing

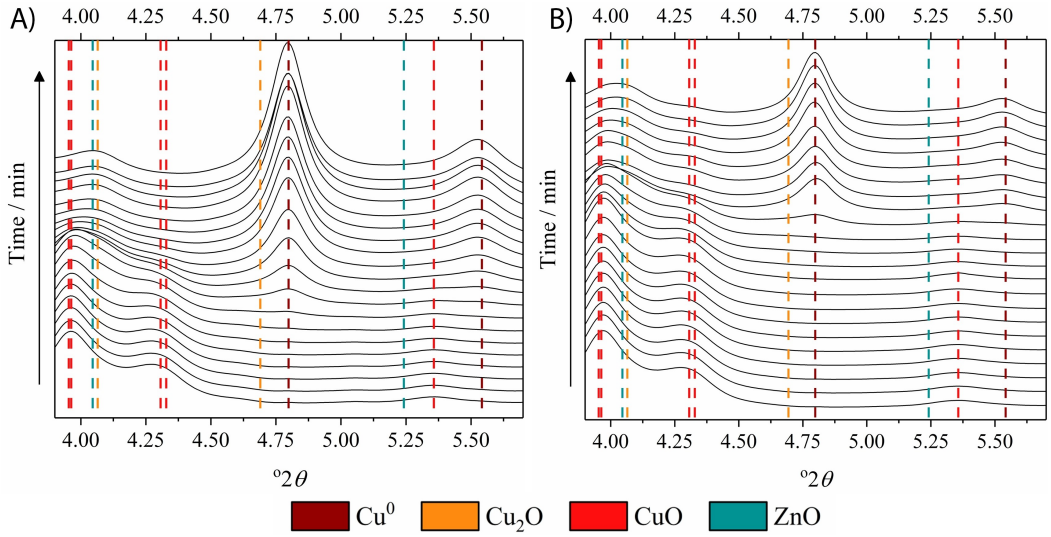

Figure 3. Time-resolved XRD data for the reduction of (A) sCZA and (B) sCZA–Cs under 5% H_2/Ar from the middle of the catalyst bed (0–70 min = 160-230 °C); the reference peak position of metallic copper (Cu^0), cuprite (Cu_2O), tenorite (CuO) and zincite (ZnO) are shown on the plots.

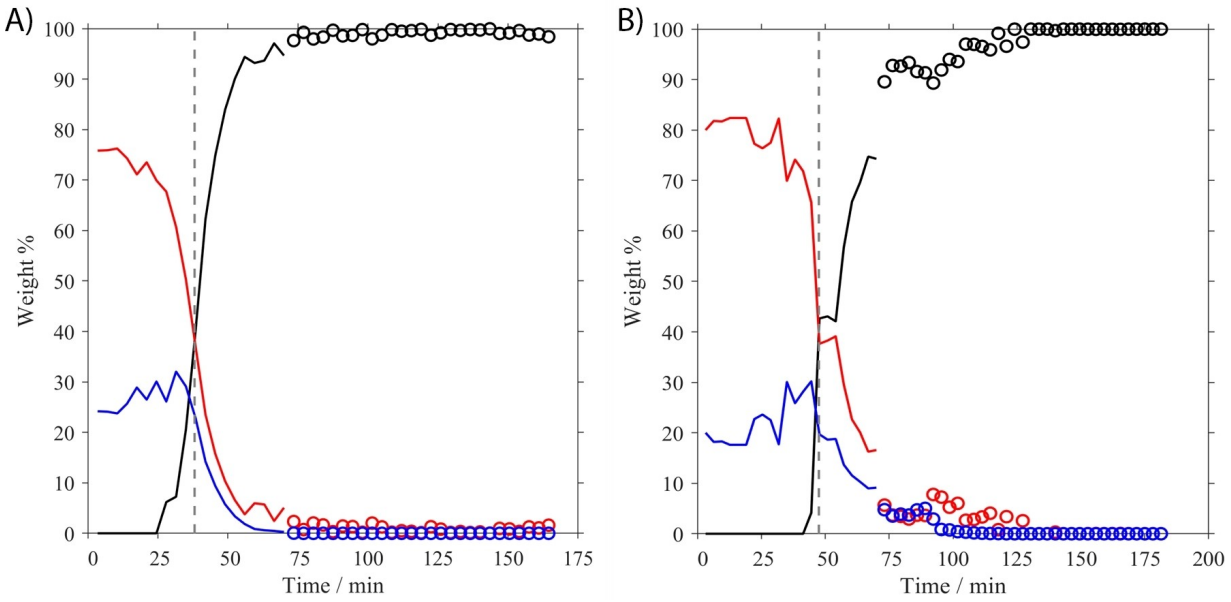

Figure 4. Cu phase evolution for in (A) sCZA and (B) sCZA–Cs during reduction in a 5% H_2/Ar environment at the middle of the catalyst bed (the top and bottom of the catalysts beds are given in Figure SI-5); the lines represent CuO (red), Cu_2O (blue) and Cu^0 (black). (0–70 min = 160-230 °C, > 70 min = 230 °C).

(Figure SI-6). The reduction of the hCZA–Cs catalyst follows a very similar profile to that of the standard catalysts reduced in a 2.5% H_2/Ar atmosphere. Again, Cs-promotion inhibits the reducibility of the Cu^0 component, but to a greater extent (i.e., takes longer).

Crystallite size analysis

There is a trend present in the effective Cu^0 crystallite sizes for the reduced sCZA and sCZA–Cs beds (shown in Figure 5 (-i) and Figure SI-10); independent of [H_2], Cu^0 D_{eff} increases towards the top of all catalyst beds (with the exception of sCZA position *(A-c)*). For the sCZA catalyst reduced under 5% H_2, the D_{eff} increases from 6.0(4) nm to 7.2(4) nm, as compared to the sCZA–Cs bed, which ranges from 6.1(4) nm to 7.7(5) nm from bottom to top. Following reduction under 2.5% H_2, the bottom of the sCZA and sCZA–Cs beds maintain a Cu crystallite size of 5.7(2) nm and 6.5(4) nm, respectively. However, this grows to 8.1(3) nm and 9.2(5) nm, respectively, at the top of the bed. It appears that the active components of the Cs-promoted catalysts incur a greater rate of sintering along the length of the bed.

Research Article
doi.org/10.1002/cmtd.202200015
Chemistry Europe
European Chemical Societies Publishing

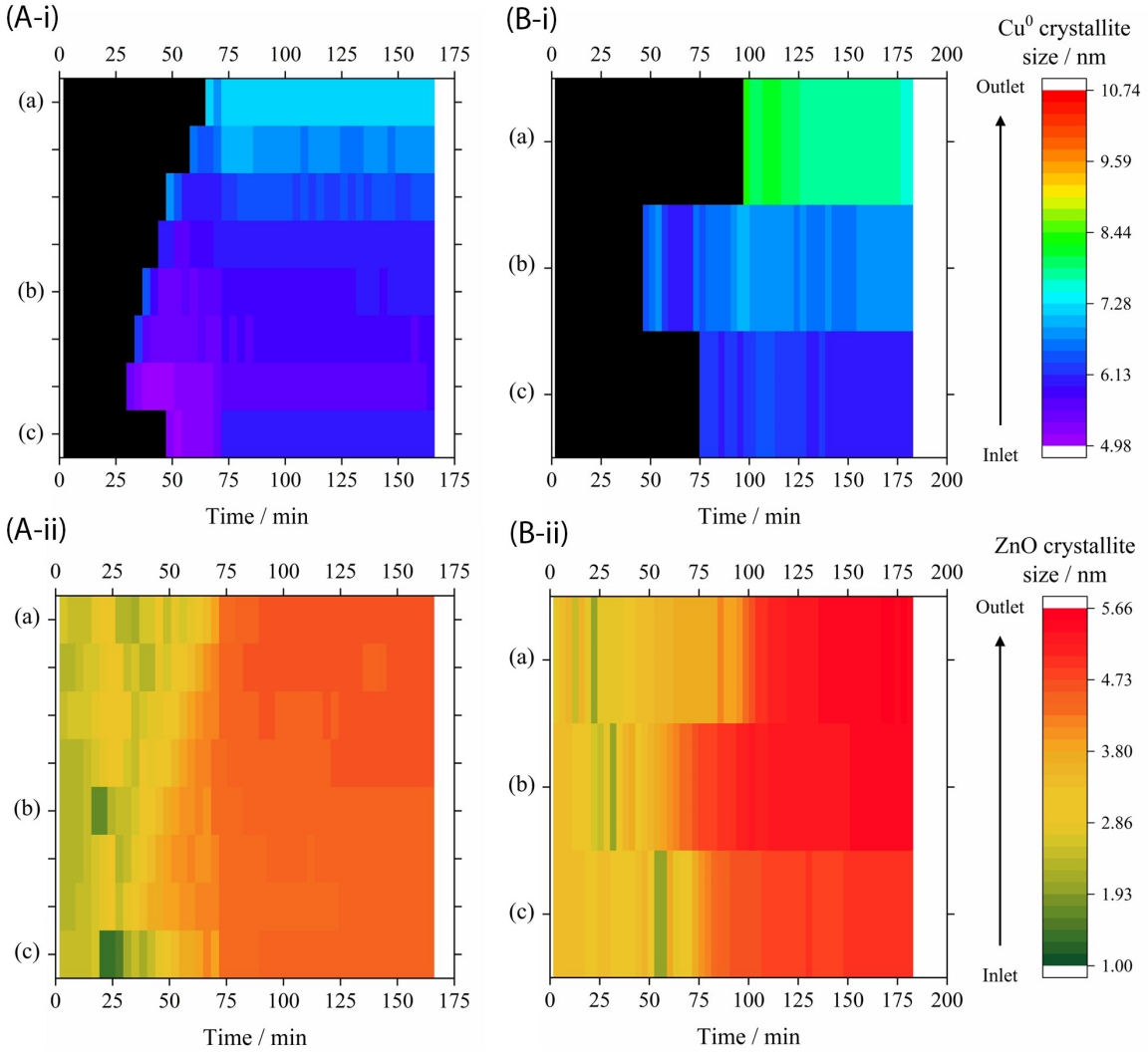

Figure 5. Effective (i) Cu^0 and (ii) ZnO crystallite sizes for (A) sCZA and (B) sCZA–Cs during reduction in 5 % H_2/Ar (0–70 min = 160–230 °C, > 70 min = 230 °C); where the (a) top, (b) middle and (c) bottom of the catalyst bed are highlighted.

Now the ZnO will be considered (see Figure 5 (-ii) and Figure SI-11). When the reducing gases are introduced (time 0 min), the ZnO apparent crystallite size is slightly larger across the standard promoted catalyst bed than the unpromoted; consistent with what was seen for the as prepared catalyst (Table 1).[38] Once reduction of the Cu-containing phases begins, a gradual increase in the ZnO domain size is seen. Interestingly, the most significant ZnO grain growth visible in Figure 5 occurs simultaneously with the reduction of CuO. The susceptibility of ZnO (wurtzite polymorph) to sinter in the presence of high partial pressures of steam is documented in the literature.[39–42] Here however, it appears that the sintering behaviour of zincite is different for the unpromoted and promoted catalysts. Irrespective of the [H_2], sintering of ZnO is more pronounced along the sCZA–Cs bed than the sCZA. There are two possible rationales for this: (1) the incipient wetness impregnation method employed promotes segregation of ZnO via HTLC formation, and/or (2) additional water is held on the surface of the promoted catalyst, facilitating further growth of ZnO.[38,43] Both scenarios require weak metal-support interactions between Cu^0-ZnO and Cu^0-Al_2O_3 as a result of phase segregation; this also accounts for the increased effective Cu crystallite sizes. Compositionally, the main difference between these two types of catalysts is Cs-promotion, therefore the role of Cs in sintering will be considered.

The incorporation of Cs-promoters in Cu-based catalysts, such as LT-WGS and methanol synthesis catalysts, has been researched.[1,44–49] Typically, the rate-determining step in the water-gas shift reaction is the dissociation of H_2O. However, once the Cu-based catalyst is promoted with 1–1.2 wt.% Cs_2O, it is reported that the dissociation of water is no longer rate-limiting and CH_3OH formation is inhibited (the latter is not explored further).[5] Evidence of Cs promoting water dissociation is reported for coverages of $\theta^*_{Cs} < 0.5$ (where a saturated monolayer of Cs atoms is described by $\theta^*_{Cs} = 1$), which corresponds to the [Cs] in the prepared catalysts; therefore, it is feasible that Cs-stabilised $OH_{(a)}$ species form in situ throughout reduction.[50,51] During operation of the low-temperature water-

gas shift reaction, it is also important to note that the optimal Cs coverage is low to prevent inaccessibility of other species to free Cu sites, for example for CO adsorption.[50]

When Cs is incorporated into the $CuO/ZnO/Al_2O_3$ catalyst, it is presumed that it preferentially chemisorbs to the Cu^0. Though it is possible for Cs to adsorb onto the O-terminated $ZnO(000\bar{1})$ and the nonpolar $ZnO(10\bar{1}0)$ surfaces, when Cu^0 is present, the majority of the promoter migrates to the Cu from the alkali-oxide interface (surface free energy $Cs = 0.067\ J\,m^{-1}$).[52,53] This is because it is more energetically favourable for Cs to donate an electron into the empty Cu(4*s*,4*p*) band than the empty Zn(4*s*,4*p*) band of ZnO. Concurrently, the valence electron in the half-occupied Cs 6*s*-orbital has a greater interaction with the occupied Cu^0 *s*-orbitals than the occupied {Zn $4s + O\ 2p$} band of ZnO. Thus, preferential adsorption of Cs on Cu occurs in the presence of ZnO, increasing the thermal stability of Cs on the surface.[52]

The sintering effects are far more pronounced for the high Cu loading catalysts (given in Figure SI-12), evidenced by the larger Cu^0 crystallite size. This is most likely due to the [ZnO] decreasing by 2/3 (from ~30 wt.% in sCZA/sCZA–Cs to ~10 wt.%). The thermal conductivity of Cu is $400\ W\,m^{-1}K^{-1}$ at room temperature, compared to $50\ W\,m^{-1}K^{-1}$ for wurtzite ZnO;[54,55] as Cu^0 has a relatively high thermal conductivity, it is more susceptible to sintering, and a role of zincite is to act as thermal stabilizer.[34] When compared to the standard catalysts reduced under identical conditions, there appears to be a trend across all results. The effective Cu^0 crystallite sizes (Figure 6 (A)) increase almost linearly from the bottom of the bed, to the top. Sintering effects are also more evident along the Cs-promoted beds as its incorporation further weakens the strong metal-support interaction (SMSI), and holds water on the surface of the Cu^0 nanoparticles, facilitating Ostwald ripening of the active component.

The dispersion of the zincite in hCZA and hCZA–Cs prior to reduction of the active component is considered intimately mixed with the tenorite, making it amorphous to diffraction (as seen in Figure 2).[16,32,33] The high extent of ZnO dispersion is maintained during the activation procedure until Cu begins reducing, which is when growth of the ZnO occurs (Figure 5 (-ii)). As previously stated, it is presumed that the water selectively hydroxylates the $ZnO(10\bar{1}0)$ surface once activation of the active component begins, promoting particle growth via Ostwald ripening.[41,56,57] These sintering effects are seen to a greater extent along the hCZA–Cs bed due to the Cs-promoter also migrating to the surface of the Cu^0 and facilitating water dissociation on the surface of the catalyst.[52]

When the final measured ZnO crystallite sizes are compared following reduction under 5% H_2 (Figure 6(B)), three conclusions can be drawn: (1) the ZnO in the high Cu loaded catalyst sinters to a greater extent (despite the larger error) due to the decreased [ZnO], (2) the larger amount of water released during reduction in the high copper loaded catalyst facilitates sintering via Ostwald ripening, and (3) the ZnO in the promoted catalyst sinters more than its unpromoted equivalent due to Cs interacting with water on the catalyst surface, hydroxylating the ZnO surfaces to a greater extent. It also appears that the particle growth mechanism occurs almost uniformly along the length of the catalyst beds, suggesting there is no obvious water build-up occurring.

Microstructural defects in copper

The conventional Williamson–Hall (cWH) method is commonly employed to evaluate the separate contribution of size and strain to overall peak broadening in a material's powder diffraction pattern as it assumes that the investigated material has uniform strain across all crystallographic directions, making it elastically isotropic.[58–60] The cWH plots calculated for all investigated catalysts (see Figures SI-13–SI-16) show a large deviation from linear regression which further affirms the presence of anisotropic strain broadening. The Full Width-Half-Maximum (FWHM)s non-monotonous 2θ-dependence is likely a result of lattice dislocations and/or twin faulting which can be

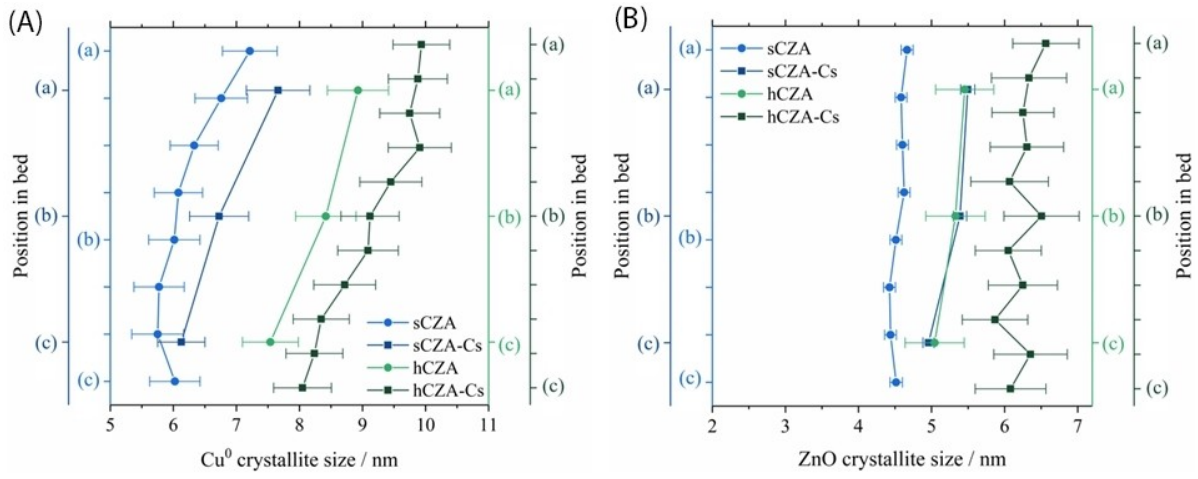

Figure 6. Effective final (A) Cu^0 and (B) ZnO crystallite sizes with errors, along the length of the catalyst beds reduced in 5% H_2/Ar; where the (a) top, (b) middle and (c) bottom positions are labelled. Note that the crystallite sizes are generally larger for the samples containing Cs and for the higher [Cu] samples.

explored further using the modified Williamson-Hall (mWH) analysis.[12,61,62]

By employing the use of average dislocation contrast factors ($\langle C_{hkl}\rangle$, see section SI-6 in Supporting Information), the dislocation affected FWHM ΔK values can be plotted as a smooth curve according to the mWH equation (Equation (2) evaluated in section SI-7).[64] It is assumed that the 12 slip-systems in the Cu face centred cubic (fcc) crystal are equally populated, and that both screw and edge dislocations occur with equal probability.[63] The mWH plots for the sCZA and sCZA–Cs catalysts reduced in 5% H_2/Ar (Figure 7) show that this method of analysing the experimental data is better suited than the cWH method. The smooth curve of the mWH plot definitively describes the anisotropic strain broadening present in the active component's microstructure as caused by structural defects. The anisotropic strain broadening is also better modelled using the mWH plot for the 1% and 2.5% H_2 activation studies of the standard catalysts, and the high copper loading catalysts reduced under 5% H_2/Ar (see section SI-7).

$$\Delta K = \frac{0.9}{D} + \left(\frac{\pi\, A^2\, b^2}{2}\right)^{\frac{1}{2}} \rho^{\frac{1}{2}} \left(K\langle C_{hkl}\rangle^{\frac{1}{2}}\right) + \left(\frac{\pi\, A'\, b^2}{2}\right) Q^{\frac{1}{2}} \left(K^2\langle C_{hkl}\rangle\right) \quad (2)$$

To determine the type of linear defects present along the catalyst beds, and whether the activation environment impacts the dislocation character, Equation (3) is employed (evaluated in section SI-8 or Equation SI-18).[65] It should be noted that the calculated values presented are representative, not quantitative.

$$\frac{[(\Delta K)^2 - \alpha]}{K^2} \cong \beta\langle C_{h00}\rangle(1 - qH^2) \quad (3)$$

The q parameters and plots of the FWHMs for the standard unpromoted and promoted catalysts reduced under 5% H_2 are given in section SI-8. The intercept of H^2 is given on the plots and corresponds to $1/q$; q values of 1.66 and 2.39 represent the pure edge and pure screw dislocations, respectively, in the {111}⟨110⟩ slip-systems. The extrapolated q values for the sCZA catalyst bed range from 2.126–2.136 (≡63.9–65.2 [screw] %), and 2.131–2.136 (≡64.5–65.2 [screw] %) for the sCZA–Cs bed. Therefore, the standard catalyst beds overall possess more screw character than edge character, with the promoted beds expressing a slightly larger concentration.

Interestingly, a predominance of screw dislocations present in a material's microstructure has been linked to a particle growth mechanism.[64,66] This mechanism is limited by the formation of steps; however, a high concentration of screw dislocations ensures the presence of step sites with kinks along them for particle growth to take place.[67] Consequently, all types of analysis preceding this section suggest the Cu^0 crystallite size increases towards the top of the catalyst bed, thus the number of screw dislocations would be expected to be greater at the top of the bed.

The FWHMs for the sCZA and sCZA–Cs catalysts reduced under 1% and 2.5% H_2 also conform to these plots. They too suggest the catalyst beds have greater [screw dislocations], as shown in Figure 8. For the unpromoted standard catalyst, the greater the [H_2], the more edge character along the length of the catalyst bed following activation. This differs from the dislocation behaviour of the standard promoted catalyst bed which does not seem as affected by the reduction environment. A clear outlier is the calculated [screw dislocation] in the middle of the sCZA–Cs bed reduced under 1% H_2; here, the [screw dislocations] greatly exceed those determined for the bottom of the bed. Pure Cu^0, when deformed at temperature, is reported to have a q value of 2.15, which is equivalent to 70.3 [screw] % (pure dislocations were given as $q_{edge} = 1.63$ and $q_{screw} = 2.37$).[61,65] It may be that, as the bed has not been completely reduced, the Cu^0 has not yet interacted with the ZnO or the Cs_2O which may afford slightly more edge character. (N.B. When copper is cold-worked, the resulting material is

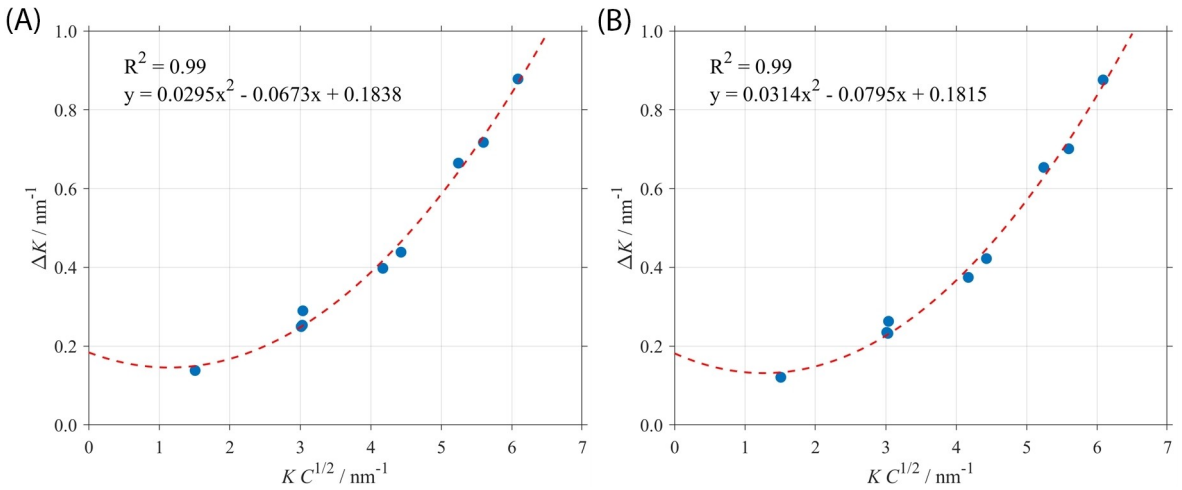

Figure 7. mWH plot for the final reduced pattern collected of the (A) sCZA and (B) sCZA–Cs catalyst reduced in 5% H_2/Ar at the middle of the catalyst bed (the mWH fits for the top and bottom of the standard catalysts beds are given in Figure SI-21 and the fits are shown in Figure SI-23).

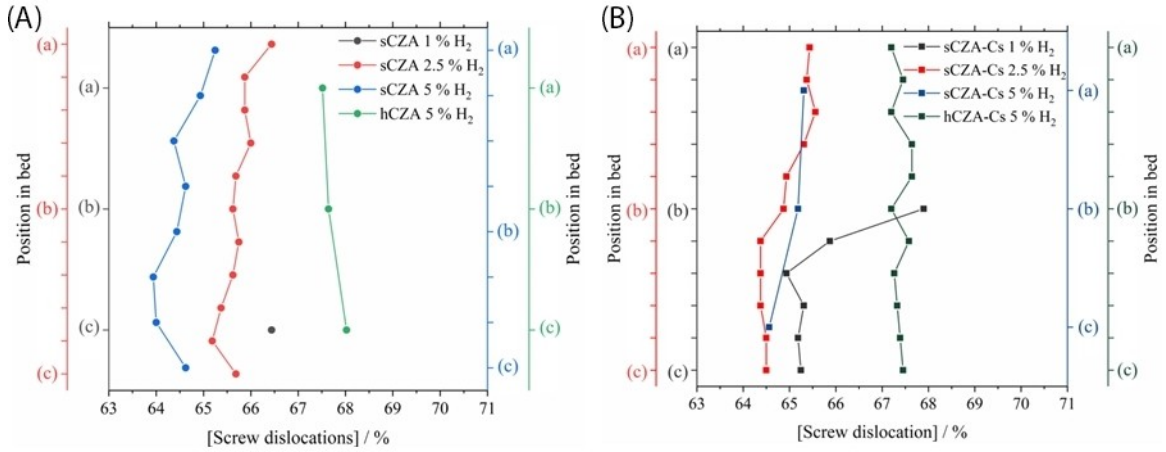

Figure 8. Graphical representation of the concentration of screw dislocations along the (A) sCZA and hCZA, and (B) sCZA–Cs and hCZA–Cs catalyst beds reduced in different [H_2]/Ar; where the (a) top, (b) middle and (c) bottom positions are labelled.

dominated by dislocations with edge character as screw dislocations are annihilated at low temperature.[17,68])

It could be that, for the sCZA catalyst bed, ZnO is more likely to partly reduce under the more forcing reducing conditions (5% H_2) making it partly migrate onto the surface of the Cu^0 due to the Cu–ZnO synergism, which is reflected in the lower [screw dislocation]. The same effect would not necessarily be seen in the promoted catalyst bed as here the promoter must also be contended with; Cs has low surface free energy and so migrates to the Cu^0 surface under any reducing conditions.

Once more, for the hCZA and hCZA–Cs catalysts reduced in 5% H_2/Ar, a good linear regression is achieved for the plots of the FWHM. The resultant experimentally determined *q* values along the length of the hCZA bed range from 2.152–2.156 (≡67.4–67.9 [screw] %), and 2.150–2.153 (≡67.1–67.5 [screw] %) for the hCZA–Cs bed.

There is little variability in the dislocation behaviour along the length of the investigated reduced catalyst beds; therefore, these microstructural defects appear to be more influenced by the interaction of the ZnO support (and Cs promoter) with the Cu^0 active component than temperature. These results suggest there is a predominance to dislocations with screw character in these LT-WGS materials, with the higher copper loading catalysts appearing to have more than the standard catalysts (Figure 8). It is hypothesised that this is due to the differing [ZnO] affecting the nature of the catalyst surface, that is, the higher the [ZnO], the more dislocations with edge character.

Phase defects visible in powder-diffraction arise from global shifts in a crystal's structure induced by both stacking faults and dislocations. However, where dislocations are caused by long-range heterogeneous strain fields, stacking faults are induced by elastic strain, affecting only the reflections within range of the fault.[69] The intensity distribution of a given Bragg reflection in a powder-pattern is dependent on its multiplicity, *j* (see section SI-9). For an ideal crystal, each peak is comprised of a number of symmetry-equivalent sub-reflections, equal to *j*, that contribute to the observed profile in the diffraction pattern.[70] However, for materials affected by stacking defects, specific selection rules determined by the *hkl* indices of the sub-reflections elucidate their influence on the resulting diffraction line profile.[71]

In order to determine the type of stacking fault formed in the slip-plane as a result of either Shockley or Frank partial dislocations, the {111}, {200}, {222} and {400} reflections must be considered. Table SI-11 evaluates the sub-reflection profiles for each reflection in terms of unbroadened (0) and broadened (±) sub-profiles, and these values are used to determine the direction of the peak shift when the deformation fault is intrinsic; the calculated constants for a given *hkl* plane, X_{hkl}, due to faulting are given in Table SI-12. For extrinsic stacking faults, the observed peak shifts occur in the opposite direction, whereas the displacements of the sub-reflections affected by twin stacking faults are negligible.[71–73]

The shift in peak position due to faulting is typically quite small; evaluating single peaks thus incurs more errors, making it advisable to evaluate a pair of reflections with opposite displacements; as shown in Table SI-10, the (1 1 1)-(2 0 0) pair and (2 2 2)-(4 0 0) pair are ideal. However, despite the calculated $\Delta(2\theta_{200}-2\theta_{111})$ being smaller than the $\Delta(2\theta_{400}-2\theta_{222})$, it is considered more accurate to use the first order reflection pair. This method is usually employed to determine the deformation (intrinsic) fault probability for α-brass (Cu/Zn 70/30); as the {111} and {200} reflections move towards each other, the stacking fault probability increases.[72,74,75] Generally, intrinsic stacking faults are solely considered for these systems as it is possible to produce vacancies following heating of the sample. To obtain a catalyst with a sufficient concentration of interstitials, external work must be done on the crystal, which has not been explored.[76]

In order to determine the stacking fault probability along the length of the standard unpromoted and promoted catalyst beds, the positions, and thus displacements, of the {111} and {200} reflections are investigated. From the time-resolved (1 1 1)-(2 0 0) peak separations displayed in Figure 9, it appears that as the bed reaches complete reduction, the $\Delta(2\theta_{200}-2\theta_{111})$

Research Article
doi.org/10.1002/cmtd.202200015
Chemistry Europe
European Chemical Societies Publishing

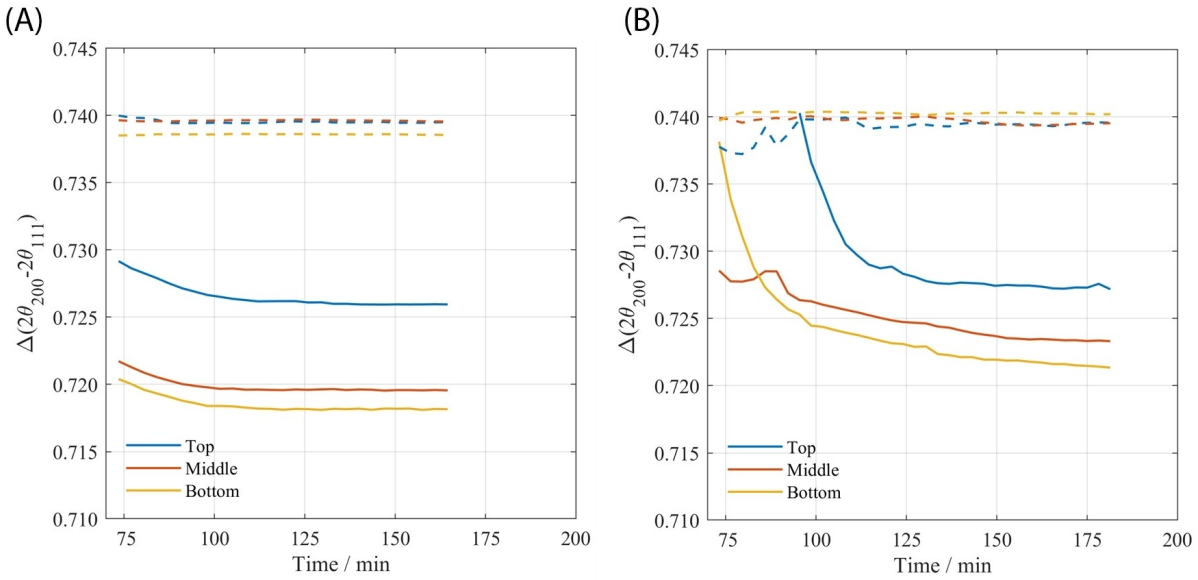

Figure 9. Time-resolved (1 1 1)-(2 0 0) peak separations for (A) sCZA and (B) sCZA–Cs activated in 5% H_2/Ar; where the dashed line represents the ideal and the solid line represents the experimentally derived difference in peak position.

deviates further from the ideal difference, eventually plateauing when complete reduction is achieved. The ideal peak position of the {111} and {200} reflections are determined by the Rietveld calculated lattice parameter, *a*, for Cu^0; this suggests that initially the active Cu^0 component does not contain defects from stacking faults, it is only as the reduction continues that intrinsic stacking faults appear. Perhaps this is a result of the ZnO partially reducing and migrating onto the Cu^0 nanoparticle's surface.[10] Across both the sCZA and sCZA–Cs beds, the difference in peak separation between the {111} and {200} reflections is smallest at the bottom. This suggests that the concentration of stacking fault increases from the top of the bed, to the bottom.

The change in peak separation between the {111} and {200} reflections for the sCZA and sCZA–Cs catalyst beds reduced in 1% and 2.5% H_2 are given in Figure SI-26 as a function of time. The trend in stacking fault probability along the length of all investigated activated standard catalyst beds is better graphically presented in Figure 10. On first inspection, it seems the higher the [H_2], the greater the fault probability; however, the (111)-(200) peak separation as a function of time decreased before plateauing once reduction was complete, and as lower hydrogen partial pressure studies were either not left long enough to fully activate the length of the bed (1% H_2) or the formation of stacking faults was still occurring as the experimental $\Delta(2\theta_{200} - 2\theta_{111})$ continued to decrease (1% and 2.5% H_2), this trend must be verified.

From Figure 10, the inverse of the stacking fault probability affords the frequency of a stacking fault once every *x* layers in the [111]-direction.[72] The variable '*x*' has been calculated for the *(a)* top, *(b)* middle and *(c)* bottom of the sCZA and sCZA–Cs beds and is presented in Table 2. It appears that stacking faults

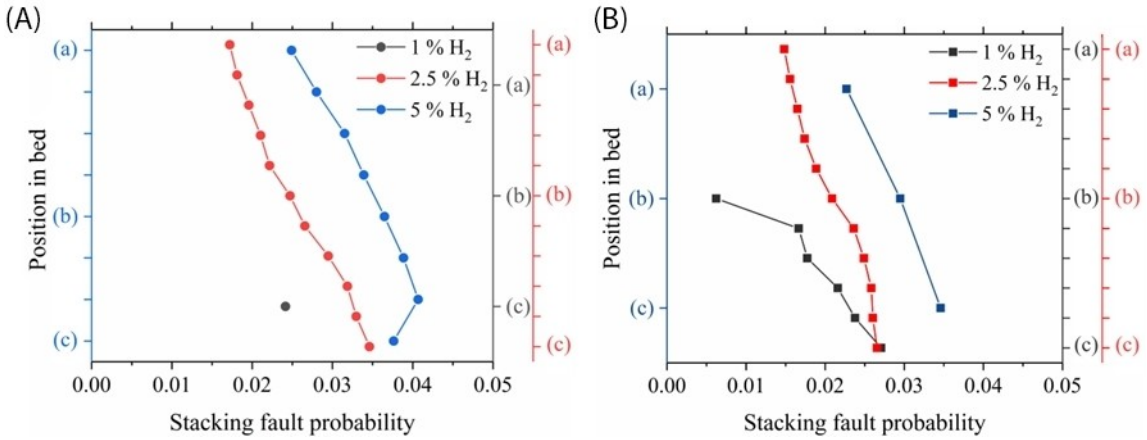

Figure 10. Distribution of stacking fault probabilities along the (A) sCZA and (B) sCZA–Cs catalyst beds following activation under 1%, 2.5% and 5% H_2/Ar; where the (a) top, (b) middle and (c) bottom positions are labelled.

Table 2. Frequency of stacking faults per x layers for the sCZA and sCZA–Cs catalysts following activation.[72]

Position in bed	sCZA [H_2]/[%]			sCZA–Cs [H_2]/[%]		
	1	2.5	5	1	2.5	5
[a] top		59	40		67	44
[b] middle		41	27	157	48	34
[c] bottom	42	29	27	37	37	29

appear more frequently throughout the standard unpromoted catalyst bed when compared to that of the promoted equivalent. The more forcing reducing atmosphere of 5% H_2 also seems to promote partial dislocation formation, and consequentially stacking faults.

A similar trend is visible for the {111} and {200} reflections in the high copper loading catalysts (see Figure SI-27). B. E. Warren and E. P. Warekois show that as the [Zn] in α-brass increases, so does the stacking fault probability. They supposed that this results from zinc incorporation reducing the energy difference between fcc and hexagonal close-packed (hcp) packing.[74] As shown in Figure 11 (and Table SI-13), a greater [Zn] leads to a greater concentration of intrinsic stacking faults (which may also be related to dislocations with more edge character).

Cs-promotion appears to reduce the stacking fault probability along the length of the standard and high Cu-loaded beds. This may be due to the body-centred cubic (bcc) arrangement of Cs, which does not possess close-packed planes.[77]

Substitutional impurities

One of the possible types of lattice point defects, substitutional impurities has not yet been investigated. Not to be confused with extrinsic point defects (interstitials), a substitutional solid solution is formed when a solute atom occupies the site of a host atom.[78] It is believed that Zn is incorporated into the Cu matrix via step sites.[10,79–82] These surface steps are generated at the intersection between Cu^0 nanoparticle surfaces and stacking faults (or twin boundaries).[80] As previously discussed, a prevalence for screw dislocations also ensures the presence of step sites.[67] Once the Zn atom is at the Cu step, it is stabilised by bulk defects in the host matrix, allowing for alloying to take place.[83] This behaviour is facilitated by SMSI via the formation of oxygen vacancies at the Cu/ZnO interface (see section SI-10).[84,85]

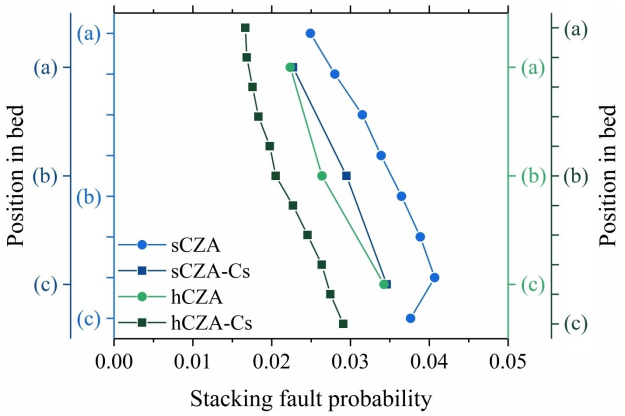

Figure 11. Comparison of the calculated stacking fault probabilities along the standard and high copper loading catalyst beds reduced under 5% H_2/Ar; where the (a) top, (b) middle and (c) bottom positions are labelled.

Using Vergard's law, the calculated lattice parameters can be evaluated to determine whether zinc has dissolved into the copper matrix during reduction.[86] The solubility limit of Zn in Cu is ~38.95 wt.% at high temperature; however, the compositional range at which stable Cu–Zn solid solutions are formed is $5.4 \leq [Zn]/wt.\% \leq 37.5$ $(5.3 \leq [Zn]/at.\% \leq 36.8)$. Interestingly, the enthalpy of mixing for these materials is negative, $\Delta H_{Cu-Zn} = -6\ kJ\,mol^{-1}$.[87] The compositional maximum concentration of ZnO incorporated into the investigated catalysts (standard) is close to 30 wt.%; for a Cu–Zn alloy with <35 wt.% Zn a stable FCC α-brass phase is exhibited, whereas above this the β-brass phase (CsCl type) is formed.

As the temperature along the bed is not monitored in situ, it is not possible to quantitatively evaluate the Cu^0 unit cell parameters for Zn-incorporation; however, assuming the temperature of the final measured diffraction pattern is 230 °C, the calculated lattice expansion and experimental lattice parameters have been plotted for the unpromoted and promoted standard catalysts in Figure 12. The outlier at the bottom of the sCZA bed reduced under 5% H_2 corresponds to a [Zn] of 2.64 at.%. Other than this result, sCZA and sCZA–Cs activated under 5% H_2 suggest <1 at.% Zn has dissolved into the Cu^0 lattice. The 2.5% H_2 activation results differ depending on the presence of Cs-promoters, with the sCZA–Cs bed suggesting a maximum [Zn] of 1.76 at.% compared to 1.03 at.% for the sCZA bed. Though the 1% H_2 studies have been included, their results are not indicative of the composition of a fully reduced catalyst bed under these conditions.

For the high Cu-loaded catalysts, the calculated atomic [Zn] exceeds that of the equivalent standard catalysts (see Figure 13). The maximum [Zn] incorporated into the hCZA Cu^0 lattice is 2.60 at.%, compared to 1.62 at.% for the hCZA–Cs catalyst. There does not appear to be an obvious relationship between Cs-promotion and the substitutional alloy formation; however, as previously introduced, these catalysts are more sensitive to changes in temperature due to their thermal conductivities which may be reflected in these results.

Lattice expansion as a result of Zn-incorporation, even at 1 at.%, distorts the host lattice quite considerably, despite the Seitz radius of zinc being comparable to Cu.[88,89] Caesium has a Seitz radius 216% larger than Zn, therefore it has been

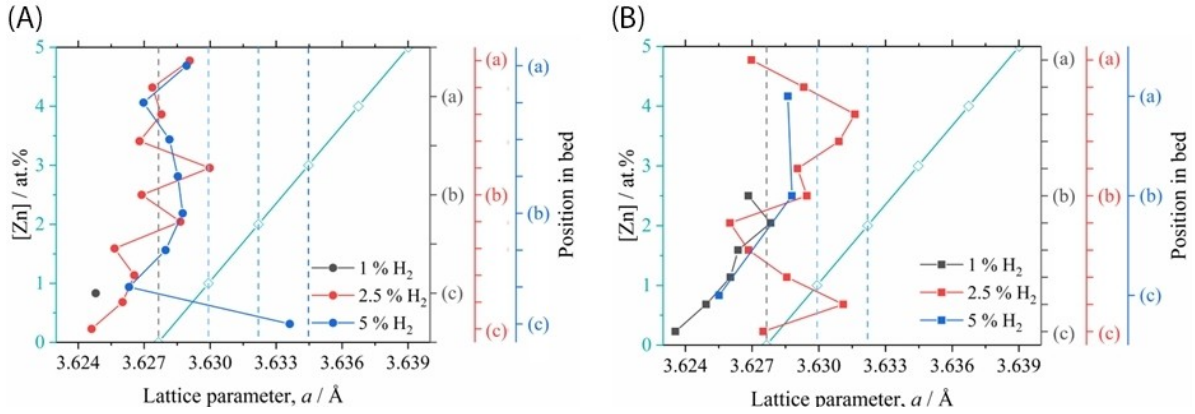

Figure 12. Graphical representation of the final calculated Cu^0 lattice parameters along the (A) sCZA and (B) sCZA–Cs beds; the dashed grey line represents the calculated Cu^0 unit cell parameter, a, at 230 °C, and the subsequent dashed blue lines correlate with the atomic [Zn].

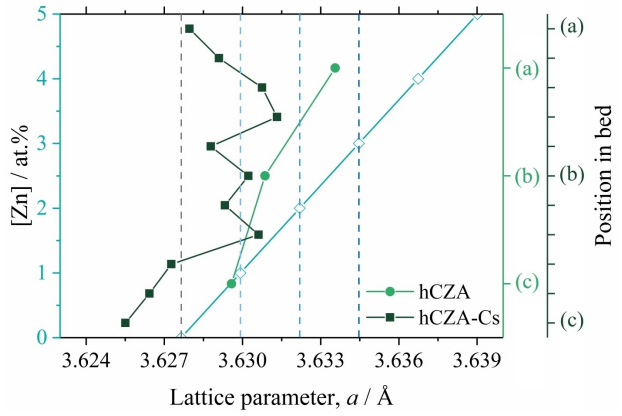

Figure 13. Graphical representation of the final calculated Cu^0 lattice parameters along the hCZA and hCZA–Cs beds; the dashed grey line represents the calculated Cu^0 unit cell parameter, a, at 230 °C, and the subsequent dashed blue lines correlate with the atomic [Zn].

concluded that Cs does not dissolve into the Cu^0 matrix.[89] There is also no evidence in the literature that Cs forms an alloy with Cu under the investigated reducing atmospheres.[52,90]

Ambient pressure X-ray photoelectron spectroscopy (APXPS) was employed to explore the surface of the sCZA and sCZA–Cs catalysts during reduction. In particular, the behaviour of the ZnO support was investigated in order to determine whether evidence of surface alloying could be detected under activation conditions. The XPS results of the Cu 2p and Zn 2p regions for the sCZA and sCZA–Cs catalysts following reduction are shown in Figure SI-29 (A) and (B). The X-ray photoelectron spectra show that the copper is completely reduced following activation as evidenced from absence of satellite peaks ~945–940 eV corresponding to Cu^{2+} and from Cu LMM Auger peaks;[91] the binding energy (BE) of Cu $2p_{3/2}$ is ~932.7 eV and for Cu $2p_{1/2}$ is ~952.5 eV for both catalysts. This is further evidence that Cs adsorbed on the surface of the sCZA–Cs catalyst does not form an alloy during reduction as the Cu 2p features remain the same.[52] The Cu LMM Auger spectra for the standard catalysts can be found in Figure SI-30 and confirms that the active component is reduced.

From Figure SI-29 (B), the BE of Zn $2p_{3/2}$ is ~1022.3 eV and for Zn $2p_{1/2}$ is ~1045.5 eV for both the unpromoted and promoted standard catalyst. Unfortunately, it is harder to evaluate the oxidation state of Zn via XPS as for Zn^0 and ZnO, the Zn $2p_{3/2}$ lines appear at 1021.4 eV and 1021.7 eV, respectively. However, the Zn $2p_{3/2}$ peak for sCZA–Cs appears broader than that of sCZA, which may indicate the presence of additional Zn species. In order to determine whether any reduction of zinc occurs, the Zn LMM Auger peak must be considered, as a 3 eV downward shift of BE (i.e. 3 eV upward shift in KE) is observed on reduction.[83]

The Zn LMM Auger lines, shown in Figure 14, suggest that the majority of the Zn remains in the Zn^{2+} state (Zn LMM peaks at ~987.0 eV in kinetic energy); however, there is evidence that a fraction of the ZnO is reduced to metallic Zn by the appearance of the shoulder at ~990.5 eV. S. Kuld et al. published similar data for such systems and attributed the Zn Auger shoulder feature as evidence for Cu/Zn alloy formation.[83] It appears the Cs-promoted sample contains a larger portion of metallic Zn than sCZA; it has been reported by S. Chaturvedi et al. that Cs cannot achieve bulk reduction of ZnO to Zn^0, but it is able to form a sub-stoichiometric zincite, ZnO_x.[52] Therefore, it is proposed that the Cs-ZnO relationship paired with the Cu-ZnO synergism promotes reduction of ZnO.

The Cs 3d region was also recorded for the promoted standard catalyst and is shown in Figure SI-31. The appearance of the Cs $3d_{5/2}$ (~725.0 eV) and Cs $3d_{3/2}$ (~739.0 eV) signals in the sCZA–Cs spectra following reduction confirm the presence of the Cs-promoter on the catalyst surface.[52]

It is important to note that the presented XP Spectra were collected following activation in a 100% H_2, strongly reducing atmosphere (at 220 °C). Under the investigated LT-WGS reduction environments ($[H_2]$ = 1%, 2.5%, 5%), ZnO reduction would not be expected to such a large extent; however, these measurements confirm the synergistic relationship between Cu and Zn as it proves substitutional alloy formation is possible, making the lattice expansion attributed to the dissolution of zinc in the copper matrix more likely.

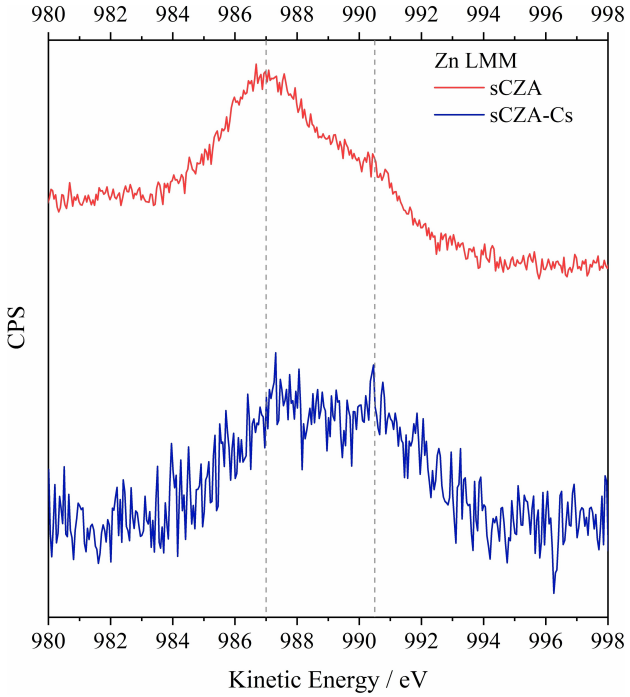

Figure 14. Zn LMM Auger spectra of sCZA and sCZA–Cs following reduction.

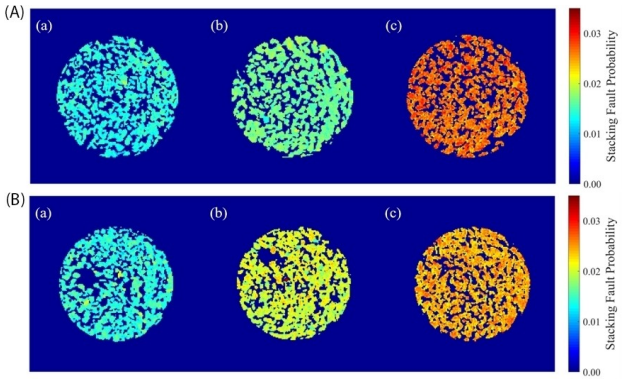

Figure 15. Stacking fault probabilities across the (a) top, (b) middle and (c) bottom of the (A) sCZA and (B) sCZA–Cs catalyst bed reduced under 5% H_2.

Application of XRD-CT

A known limitation of XRD is that it is a volume averaged measure of the crystalline component of a sample and therefore only measures an average of the point at which the catalyst bed is being interrogated. To overcome this, XRD-CT has been employed to afford an image consisting of 27000 unique diffraction patterns across the plane of the bed; these spatially-resolved patterns offer more information concerning the microstructure of the active Cu component following activation when compared to the point measurements.

It is proposed that, as for methanol synthesis catalysts, the microstructure of the catalyst determines its intrinsic activity: the greater the stacking fault probability, the more active for catalysis.[10] To the best knowledge of the author, this is the first example of this type of analysis being applied to time-resolved XRD, as well as spatially-resolved XRD-CT, of copper-based LT-WGS catalysts.[10,92,93]

The distribution of stacking fault probabilities across the three interrogated planes of the sCZA and sCZA–Cs catalyst beds reduced under 5% H_2 are shown in Figure 15. The *(c)* bottom of both beds contains a much larger α than the *(a)* top and *(b)* middle positions; Cs-promotion appears to decrease α here. However, this behaviour is reversed in the middle of the catalyst beds with sCZA–Cs exhibiting greater α. For the beds reduced in 1% and 2.5% H_2, α decreases from the *(c)* bottom of the bed to the *(a)* top, with the sCZA beds appearing more active (refer to section SI-11).

Sintering plays a key role here: the smaller the Cu^0 crystallite size, the greater the stacking fault probability. The chief motive for particle rearrangement during sintering is to minimise the excess surface free energy:[94] as the surface defects are consumed, surface diffusion decelerates.[95] If the temperature profile follows the grain growth behaviour – increases from the *(c)* bottom of the bed to the *(a)* top – it appears the formation of SFs favours lower temperatures. It would thus be expected that the bottom of both standard beds would have greater WGS activity as a result of this.

Dissolution of Zn into the Cu host matrix has been shown to be possible for catalysts of these compositions. Paired with the *(a)* top of the bed (outlet) being open to the atmosphere, it is possible these stacking fault probability plots would also correlate with stacking fault energy.[96] The larger oxygen content at the top of the reactor would inhibit partial reduction of the zinc, minimising the available oxygen vacancies, and increasing the Cu-ZnO interface free energy (reduced SMSI). In comparison, the *(c)* bottom of the bed receives the reducing gas free of any oxidants, allowing partial reduction of the Zn to occur, decreasing the interface energy and promoting substitutional surface-alloy formation.[97] Along the length of the bed, water released during activation hydroxylates the ZnO($10\bar{1}0$) surface promoting grain growth of the ZnO support, further reducing the [α].[41,56,57]

The average stacking fault frequency per *x* layers have also been calculated and displayed in Table 3 to highlight the amount of information shown across the XRD-CT planes and the issues with bulk measurements. For reference, M. Behrens et al. found that an active $CuO/ZnO/Al_2O_3$ (60/30/10) catalyst for MeOH synthesis had an α of ~0.018, which corresponds to a SF in the stacking of the (1 1 1) layers once every 56 layers.[10,72]

Table 3. The average frequency of SFs per x layers, as calculated from the XRD-CT, for the standard and high Cu loading catalysts reduced under 5% H_2/Ar.[72]

Position in bed	Frequency of SFs per *x* layers			
	sCZA	sCZA	hCZA	hCZA-Cs
[a] top	72	72	76	104
[b] middle	60	60	59	50
[c] bottom	38	38	48	61

On first inspection of the distribution of stacking fault probabilities across the unpromoted and promoted high Cu-loaded catalyst beds (see Figure 16), the higher [Cu^0] (or the lower [ZnO]) is detrimental to the formation of stacking faults. Following the explanation for the standard catalysts, this appears to be a result of weak metal-support interactions between Cu^0 and ZnO reducing stacking fault formation. The *(A-c)* bottom of the hCZA bed contains the greatest stacking faut density suggesting that Cs has a greater effect on these systems. Interestingly, the α appears quite uniform across the *(B-b)* middle and *(B-c)* bottom of the hCZA–Cs bed, perhaps indicating that the maximum number of SFs have been formed.

Summary and Conclusions

In summary, the work presented has described how greater edge character of dislocations and subsequent stacking fault probability, α, is dependent on higher [H_2], smaller Cu^0 (and ZnO) crystallite size, increased [ZnO] (30 wt.%, sCZA) and on lower temperature; it is expected that these microstructural properties would increase their water-gas shift activity. Cs-promotion of these catalysts does not appear to impact the microstructure of the active Cu^0 component greatly, although it does promote sintering, and may inhibit the promotional effects of the zincite ZnO.

It has been shown that the Cu^0 lattice defects, in particular stacking faults, arise as the reduction occurs. This can be attributed to both the dissolution of Zn in the host Cu matrix, as well as the increased [H_2] facilitating the partial reduction of Zn. It is proposed that the Cu-ZnO synergism promotes the formation of dislocations with more edge character, making ZnO a key microstructural component which contributes towards thermal stability and catalyst behaviour.

When the impact of the Cs promoter is considered, its role as an electronic promoter appears to predominantly effect the early onset deactivation, whereby its incorporation as a promoter increased the sintering effects of the active component. It was determined that this was due to Cs preferentially chemisorbing to the surface of the Cu^0 and promoting water dissociation on the catalyst surface. Despite the AP-XPS studies suggesting reduction of the ZnO support is facilitated by the addition of Cs, the electronic properties of the Cs-promoter ultimately dampen its promotional effects.

To conclude, via XRD and XRD-CT it was determined that α increases with increasing Zn content via SMSI (this is inferred from the AP-XPS data), and that Cs-promotion impacts this, not only by causing sintering of the active component and thus reducing the stacking fault probability, but also by inducing further growth of the zincite crystallites, reducing any SMSI which inhibits formation of the ZnO_x overgrowth. Future work will examine the impact of these subtle differences in microstructure on WGS performance.

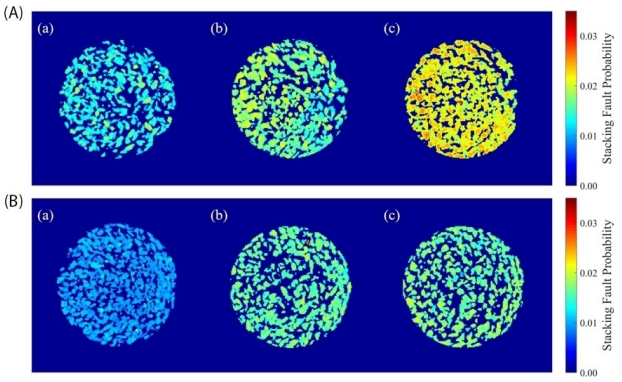

Figure 16. Stacking fault probabilities across the (a) top, (b) middle and (c) bottom of the (A) hCZA and (B) hCZA–Cs catalyst bed reduced under 5% H_2.

Experimental Section

Synthesis

The sCZA and hCZA hydroxycarbonate precursors were synthesised via coprecipitation. Using a Metrohm Titrando, the Cu, Zn, Al (sCZA = 60/30/10 and hCZA = 80/10/10) nitrate solution (1 M, 160 mL, 5 mL min^{-1}) and Na_2CO_3 (1.2 M) precipitating agent were dosed into DI H_2O (800 mL, 18.2 MΩ cm^{-1}) heated to 65 °C. The mother liquor was aged for 1.5 h at 65 °C and pH 7 under vigorous stirring. The precipitate was then filtered, washed and dried in air at 80 °C for 15 h. The promoted catalysts (sCZA–Cs and hCZA–Cs) were prepared via incipient wetness impregnation. The sCZA and hCZA precursors were impregnated with a solution of ~1 wt.% Cs_2CO_3 (determined by pore volume). These were then dried in air at 80 °C for 15 h. All catalyst precursors were calcined in air at 300 °C (2 °C min^{-1}) for 5 h. The calcined sCZA, sCZA–Cs, hCZA and hCZA–Cs catalysts were compressed into a 13 mm disc using a hydraulic press (Specac Ltd., UK), then crushed and sieved (125-250 μm).

Ex situ characterisation

Infrared (IR) spectra were recorded with a Thermo Scientific Nicolet iS 10 FTIR spectrometer at a spectral resolution of 2 cm^{-1}, accumulating 64 scans.

Chemical compositions of the catalyst samples were determined by X-ray fluorescence (XRF). This was measured using a PANalytical Epsilon 3-XL spectrometer at the ISIS Materials Characterisation laboratory, Harwell, UK, and analysed using Epsilon 3 software.

Using a Mettler-Toledo TGA/DSC 1 Star TGA at Yara International, Porsgrunn, NO, the thermogravimetric analysis (TGA) was conducted in a flow of air at a heating rate of 20 °C min^{-1} from room temperature to 900 °C, with an isothermal time of 90 min. Evolved gas analysis (EGA) was carried out with a Pfeifer Thermostar GSD 320 T2 mass spectrometer (MS).

Temperature-programmed reduction (TPR) experiments were carried out in a ChemBET *Pulsar* TPR/TPD instrument, which is a Quantachrome automated chemisorption analyser. The operating variables (S_0, F, C_0 and β) were chosen to ensure $0.9 < K < 2.3$ min and $P < 20$ K were satisfied.[98,99] Each sample was heated to 400 °C (10 °C min^{-1}) in 30 mL min^{-1} of 10% H_2/Ar. The amount of sample reduced was dependent on the [Cu] in the investigated catalyst.

X-ray diffraction (XRD) measurements were collected with $Cu_{K\alpha 1}$ ($\lambda = 1.5404$ Å) radiation using an accelerating voltage/current of 40 kV/40 mA respectively on a Bruker D8 Advance powder diffractometer equipped with a Vantec-1D-Linear detector at Diamond

Light Source (DLS), Harwell, UK. The diffractograms were recorded using DIFFRAC^{plus} XRD Commander software in a locked coupled continuous mode between 5–60 °2θ with a step size of 0.017°. 1.0 mm divergence and 0.6 mm detector slits were used for all scans. Phase identification of the patterns was carried out using PANalytical X'Pert HighScore Plus.

AP-XPS measurements collected at B07, DLS

In situ ambient-pressure X-ray photoelectron spectroscopy (AP-XPS) experiments were performed at Versatile Soft X-ray (VerSoX) beamline B07 at Diamond Light Source.[100] The VerSoX APXPS end station is equipped with a differentially pumped PHOIBOS 150 NAP hemispherical electron energy analyser, which allows in situ measurements in mbar range. In the geometry adopted during the experiments, photoelectrons were detected at an angle of 54.7 ° with respect to the direction of the surface normal, and linearly polarized light was used throughout the experiments. The spectra were energy calibrated using C 1s at 285.0 eV and were normalised at the maximum intensity.

The authors provided the sCZA and sCZA–Cs catalysts in powder form, which were then dispersed as a thin film on a gold coated silicon wafer with an area of ~0.5 cm^2. The wafer was fixed to the sample holder with stainless steel clips. The catalysts were heated (10 °C min^{-1}) in resistive mode, and the temperature was monitored with a Type-K (chromel-alumel) thermocouple integrated into the sample holder. Within the Tea Cup reaction chamber (0.7 L), the catalysts were reduced in H_2 (50 mbar) at 220 °C for 1 h, and then the pressure was evacuated (1 mbar) and spectra were measured with 1700 eV excitation. Ultrapure gases were utilized, which were introduced through precision leak valves.

XRD and XRD-CT measurements collected at ID15 A, ESRF

In situ synchrotron X-ray diffraction and XRD-computed tomography (CT) measurements were collected at the ESRF on beamline station ID15 A using a 70 keV monochromatic X-ray beam with a 30×20 μm (H×V) spot size (λ = 0.17463 Å). The detector used to collect the 2D diffraction patterns was a Dectris Pilatus3 X CdTe 2 M (1475×1679 pixels, pixel size of 172×172 μm) hybrid photon counting area detector. The beam was calibrated using a CeO_2 NIST standard.

The catalytic reactor set-up consisted of the $CuO/ZnO/Al_2O_3$(-Cs_2CO_3) catalyst (0.3 g, bed length of 1.9 cm) supported on quartz wool in a 4.5 mm quartz capillary. This was then mounted into a gas delivery stub, which was attached to a standard goniometer on a rotation and translation stage. The furnace was lowered to cover the sample tube and heat the catalytic reactor from all directions, from ambient up to 230 °C at atmospheric pressure. The gas inlet was placed at the bottom of the bed and the top of the bed was open to the atmosphere. Prior to the beamtime experiments, temperature calibrations were carried out in spare catalyst with a thermocouple embedded in the bed to ensure there was no obvious gradient along the bed; however, the gases were not heated as they were delivered.

To investigate the impact of the activation procedure on the resultant catalyst microstructure, each sample was first heated to 160 °C (5 °C min^{-1}) in Ar, reduced in flowing H_2 (1%, 2.5% and 5%) in Ar up to 230 °C (1 °C min^{-1}) and held at this temperature until fully reduced (or for as long as possible). The GHSV was 1985 h^{-1}. Two gas bottles were used containing a 5% H_2/Ar mix and 100% Ar. The gas flow rate (10 mL min^{-1}) was controlled by two MFCs (Alicat MC-10SCCM–D).

Point measurements were taken along the catalytic reactor bed (*Z*-scanning) at either 3 or 11 positions during the reduction ramp (160–230 °C) and during reduction (230 °C isothermal). The top, middle and bottoms heights are considered comparable across all measurements; to the best knowledge of the author, the thickness of the quartz wool was the same, the height of the sample bed was constant, therefore the temperature in the reactor cells are considered comparable. This allowed any gradient present in the catalytic bed to be evaluated at either variable position and constant time, or at variable time and constant position; the latter is how the data is presented in this paper.

XRD-CT measurements of the catalyst bed (*X*,*Y*-scanning) were collected at 3 positions, the top, middle and bottom, at the end of the reduction run (230 °C). During the measurements, the reduction was stalled by switching the gas flow to pure Ar (10 mL min^{-1}).

The parameters for the tomographic measurements were a step size of 1.2 ° to collect 180 translation steps in an angular range of 0–180° (150 line scans/projections), therefore a total of 27000 2D powder diffraction patterns were collected for each XRD-CT scan. The physical area covered by the beam was 5.4×5.4 mm^2. These were radially integrated to give 1D powder diffraction patterns, after applying a filter that removed outliers and single-crystal diffraction artefacts using nDTomo and pyFAI software packages. A filter back projection algorithm was then employed in MATLAB to reconstruct each sinogram.[101–103] The sinograms consisted of a 3D matrix (200×200×1990 matrix) in which the 1st dimension illustrates the translation steps, the 2nd the rotation steps and the 3rd dimension shows the channels in the 1D patterns, giving a total of 1990 sinograms.

It should be noted that tan2θ broadening (parallax problem) is not considered an issue when evaluating the measured data. This is most clear when evaluating the Cu^0 crystallite size across the plane of the bed – if broadening were an issue, it would be expected that a gradient would be apparent (exemplar data has been included in SI-12 in Supporting Information).

Acknowledgements

We acknowledge funding from Yara International ASA for the PhD studentship for D.M.F. Dr. Antony Vamvakeros and Dr. Marco DiMichiel are acknowledged for their assistance in acquiring the XRD data on beamline ID15A, ESRF. We would also like to thank Gavin Stenning for help on the X-ray fluorescence instrument in the Materials Characterisation Laboratory at the ISIS Neutron and Muon Source

Conflict of Interest

The authors declare no conflict of interest.

Data Availability Statement

Raw diffraction data available on request.

Keywords: copper · defects · dislocations · microstructure · X-ray diffraction

[1] P. Kowalik, W. Próchniak, T. Borowiecki, *Catal. Today* **2011**, *176*, 144–148.
[2] Y. Li, Q. Fu, M. Flytzani-Stephanopoulos, *Appl. Catal. B* **2000**, *27*, 179–191.
[3] L. Lloyd, D. E. Ridler, M. V. Twigg, in *Catal. Handb.* (Ed.: M. V. Twigg), Wolfe Publishing Ltd, London, **1996**, pp. 283–339.
[4] M. D. Argyle, C. H. Bartholomew, *Catalysts* **2015**, *5*, 145–269.
[5] P. Kowalik, W. Próchniak, M. Konkol, T. Borowiecki, *Appl. Catal. A* **2012**, *423–424*, 15–20.
[6] C. Baltes, S. Vukojević, F. Schüth, *J. Catal.* **2008**, *258*, 334–344.
[7] I. Kasatkin, P. Kurr, B. L. Kniep, A. Trunschke, R. Schlögl, *Angew. Chem. Int. Ed.* **2007**, *46*, 7324–7327; *Angew. Chem.* **2007**, *119*, 7465–7468.
[8] M. Behrens, R. Schlögl, *Z. Anorg. Allg. Chem.* **2013**, *639*, 2683–2695.
[9] M. Behrens, *Catal. Today* **2015**, *246*, 46–54.
[10] M. Behrens, F. Studt, I. Kasatkin, S. Kühl, M. Hävecker, F. Abild-Pedersen, S. Zander, F. Girgsdies, P. Kurr, B. L. Kniep, M. Tovar, R. W. Fischer, J. K. Nørskov, R. Schlögl, *Science* **2012**, *759*, 893–898.
[11] P. Kurr, I. Kasatkin, F. Girgsdies, A. Trunschke, R. Schlögl, T. Ressler, *Appl. Catal. A* **2008**, *348*, 153–164.
[12] T. Kandemir, I. Kasatkin, F. Girgsdies, S. Zander, S. Kühl, M. Tovar, R. Schlögl, M. Behrens, *Top. Catal.* **2014**, *57*, 188–206.
[13] Z. A. D. Lethbridge, R. I. Walton, A. S. H. Marmier, C. W. Smith, K. E. Evans, *Acta Mater.* **2010**, *58*, 6444–6451.
[14] P. Scardi, M. Leoni, in *Diffr. Anal. Microstruct. Mater.* (Eds.: E. J. Mittemeijer, P. Scardi), Springer, Berlin, **2004**, pp. 51–91.
[15] C. Zener, *Phys. Rev.* **1947**, *71*, 846–851.
[16] W. M. Haynes, in *CRC Handb. Chem. Phys.* (Ed.: W. M. Haynes), CRC Press, Boca Raton, **2014**.
[17] T. Ungár, J. Gubicza, G. Ribárik, A. Borbély, *J. Appl. Crystallogr.* **2001**, *34*, 298–310.
[18] H. Trinkaus, *Phys. Status Solidi* **1972**, *51*, 307–319.
[19] D. Waller, D. Stirling, F. S. Stone, M. S. Spencer, *Faraday Discuss. Chem. Soc.* **1989**, *87*, 107–120.
[20] C. Ratnasamy, J. P. Wagner, *Catal. Rev.* **2009**, *51*, 325–440.
[21] G.-C. Shen, S. Fujita, N. Takezawa, *J. Catal.* **1992**, *138*, 754–758.
[22] P. J. Smith, S. A. Kondrat, P. A. Chater, B. R. Yeo, G. M. Shaw, L. Lu, J. K. Bartley, S. H. Taylor, M. S. Spencer, C. J. Kiely, G. J. Kelly, C. W. Park, G. J. Hutchings, *Chem. Sci.* **2017**, *8*, 2436–2447.
[23] M. Behrens, *J. Catal.* **2009**, *267*, 24–29.
[24] M. Behrens, F. Girgsdies, *Z. Anorg. Allg. Chem.* **2010**, *636*, 919–927.
[25] S. Zander, E. L. Kunkes, M. E. Schuster, J. Schumann, G. Weinberg, D. Teschner, N. Jacobsen, R. Schlögl, M. Behrens, *Angew. Chem. Int. Ed.* **2013**, *52*, 6536–6540; *Angew. Chem.* **2013**, *125*, 6664–6669.
[26] T. Yamaoka, M. Abe, M. Tsuji, *Mater. Res. Bull.* **1989**, *24*, 1183–1199.
[27] T. Baird, K. C. Campbell, P. J. Holliman, R. Hoyle, D. Stirling, B. P. Williams, *J. Chem. Soc. Faraday Trans.* **1995**, *91*, 3219–3230.
[28] C. Busetto, G. Del Piero, G. Manara, F. Trifirò, A. Vaccari, *J. Catal.* **1984**, *85*, 260–266.
[29] S. Kühl, A. Tarasov, S. Zander, I. Kasatkin, M. Behrens, *Chem. Eur. J.* **2014**, *20*, 3782–3792.
[30] U. Costantino, F. Marmottini, M. Sisani, T. Montanari, G. Ramis, G. Busca, M. Turco, G. Bagnasco, *Solid State Ionics* **2005**, *176*, 2917–2922.
[31] F. Kooli, C. Depège, A. Ennaqadi, A. de Roy, J. P. Besse, *Clays Clay Miner.* **1997**, *45*, 92–98.
[32] G. Prieto, J. Zečević, H. Friedrich, K. P. de Jong, P. E. de Jongh, *Nat. Mater.* **2013**, *12*, 34–39.
[33] A. M. Nawar, N. Abdel Aal, N. Said, F. El-Tantawy, F. Yakuphanoglu, *IOSR J. Appl. Phys.* **2014**, *6*, 17–22.
[34] M. V. Twigg, M. S. Spencer, *Appl. Catal. A* **2001**, *212*, 161–174.
[35] D. Ectors, F. Goetz-Neunhoeffer, J. Neubauer, *J. Appl. Crystallogr.* **2015**, *48*, 189–194.
[36] J. Y. Kim, J. A. Rodriguez, J. C. Hanson, A. I. Frenkel, P. L. Lee, *J. Am. Chem. Soc.* **2003**, *125*, 10684–10692.
[37] J. A. Rodriguez, J. Y. Kim, J. C. Hanson, M. Pérez, A. I. Frenkel, *Catal. Lett.* **2003**, *85*, 247–254.
[38] A. J. Marchi, C. R. Apesteguía, *Appl. Clay Sci.* **1998**, *13*, 35–48.
[39] J. C. J. Bart, R. P. A. Sneeden, *Catal. Today* **1987**, *2*, 1–124.
[40] D. Dollimore, P. Spooner, *Trans. Faraday Soc.* **1971**, *67*, 2750–2759.
[41] J. A. Varela, O. J. Whittemore, E. Longo, *Ceram. Int.* **1990**, *16*, 177–189.
[42] A. Prašnikar, A. Pavlišič, F. Ruiz-Zepeda, J. Kovač, B. Likozar, *Ind. Eng. Chem. Res.* **2019**, *58*, 13021–13029.
[43] M. B. Fichtl, D. Schlereth, N. Jacobsen, I. Kasatkin, J. Schumann, M. Behrens, R. Schlögl, O. Hinrichsen, *Appl. Catal. A* **2015**, *502*, 262–270.
[44] J. G. Nunan, K. Klier, C.-W. Young, P. B. Himelfarb, R. G. Herman, *J. Chem. Soc. Chem. Commun.* **1986**, 193–195.
[45] K. Klier, C.-W. Young, J. G. Nunan, *Ind. Eng. Chem. Fundam.* **1986**, *25*, 36–42.
[46] J. Nakamura, J. M. Campbell, C. T. Campbell, *J. Chem. Soc. Faraday Trans.* **1990**, *86*, 2725–2734.
[47] J. M. Campbell, J. Nakamura, C. T. Campbell, *J. Catal.* **1992**, *136*, 24–42.
[48] C. T. Campbell, B. E. Koel, *Surf. Sci.* **1987**, *186*, 393–411.
[49] H. N. Evin, G. Jacobs, J. Ruiz-Martinez, G. A. Thomas, B. H. Davis, *Catal. Lett.* **2008**, *120*, 166–178.
[50] C. T. Campbell, in *Chem. Phys. Solid Surfaces*, Academic Press, Inc., **1993**, pp. 287–310.
[51] J. A. Rodriguez, W. D. Clendening, J. M. Campbell, W. Min, C. T. Campbell, *J. Vac. Sci. Technol. A* **1989**, *7*, 2118–2120.
[52] S. Chaturvedi, J. A. Rodriguez, *Surf. Sci.* **1998**, *401*, 282–295.
[53] L. Z. Mezey, J. Giber, *Jpn. J. Appl. Phys.* **1982**, *21*, 1569–1571.
[54] "Thermal Conductivity of Metals, Metallic Elements and Alloys," can be found under https:// www.engineeringtoolbox.com/thermal-conductivity-metals-d 858.html, **2005**.
[55] X. Wu, J. Lee, V. Varshney, J. L. Wohlwend, A. K. Roy, T. Luo, *Sci. Rep.* **2016**, *6*, 22504.
[56] M. Y. Sengul, J. Guo, C. A. Randall, A. C. T. van Duin, *Angew. Chem. Int. Ed.* **2019**, *58*, 12420–12424; *Angew. Chem.* **2019**, *131*, 12550–12554.
[57] Y. Dai, P. Lu, Z. Cao, C. T. Campbell, Y. Xia, *Chem. Soc. Rev.* **2018**, *47*, 4314–4331.
[58] P. Barnes, S. D. M. Jacques, M. Vickers, "Determination of Size and Strain," can be found under http://pd.chem.ucl.ac.uk/pdnn/peaks/sizedet.htm, **2006**.
[59] G. K. Williamson, W. H. Hall, *Acta Metall.* **1953**, *1*, 22–31.
[60] P. M. Shafi, A. C. Bose, *AIP Adv.* **2015**, *5*, 057137.
[61] T. Ungár, G. Tichy, *Phys. Status Solidi* **1999**, *171*, 425–434.
[62] B. E. Warren, *J. Appl. Phys.* **1961**, *32*, 2428–2431.
[63] T. Ungár, in *Denver X-Ray Conf. Appl. X-Ray Anal.*, **1996**, pp. 1–14.
[64] T. Ungár, S. Ott, P. G. Sanders, A. Borbély, J. R. Weertman, *Acta Mater.* **1998**, *46*, 3693–3699.
[65] T. Ungár, I. Dragomir, Á. Révész, A. Borbély, *J. Appl. Crystallogr.* **1999**, *32*, 992–1002.
[66] F. Meng, S. A. Morin, A. Forticaux, S. Jin, *Acc. Chem. Res.* **2013**, *46*, 1616–1626.
[67] I. V. Markov, in *Cryst. Growth Beginners Fundam. Nucleation, Cryst. Growth, Ep.*, World Scientific, Singapore, **2017**, pp. 181–360.
[68] T. Ungár, J. Gubicza, P. Hanák, I. Alexandrov, *Mater. Sci. Eng. A* **2001**, *319–321*, 274–278.
[69] M. Dupraz, G. Beutier, D. Rodney, D. Mordehai, M. Verdier, *J. Appl. Crystallogr.* **2015**, *48*, 621–644.
[70] J. K. Cockcroft, "Reflection multiplicity," can be found under http://pd.chem.ucl.ac.uk/pdnn/symm2/multj.htm, **2006**.
[71] J. Gubicza, in *X-Ray Line Profile Anal. Mater. Sci.*, IGI Global, Hershey, **2014**, pp. 101–141.
[72] B. E. Warren, in *X-Ray Diffr.*, Dover Publications, Inc., New York, **1990**, pp. 251–314.
[73] A. I. Ustinov, L. O. Olikhovska, N. M. Budarina, F. Bernard, in *Diffr. Anal. Microstruct. Mater.* (Eds.: E. J. Mittemeijer, P. Scardi), Springer, Berlin, **2004**, pp. 333–359.
[74] B. E. Warren, E. P. Warekois, *Acta Metall.* **1955**, *3*, 473–479.
[75] B. E. Warren, E. P. Warekois, *J. Appl. Phys.* **1953**, *951*, 951–952.
[76] H. J. Wollenberger, in *Phys. Metall.* (Eds.: R. W. Cahn, P. Haasen), Elsevier Science B. V., Amsterdam, **1996**, pp. 1621–1721.
[77] P. Atkins, J. de Paula, in *Atkins' Phys. Chem.*, Oxford Universty Press, Oxford, **2010**, pp. 695–742.
[78] R. Phillips, in *Crystals, Defects Microstruct. Model. Across Scales*, Cambridge University Press, Cambridge, **2001**, pp. 311–361.
[79] M. R. Gogate, *Pet. Sci. Technol.* **2019**, *37*, 671–678.
[80] J. P. Greeley, *Science* **2012**, *336*, 810–811.
[81] S. Kuld, M. Thorhauge, H. Falsig, C. F. Elkjær, S. Helveg, I. Chorkendorff, J. Sehested, *Science* **2016**, 969–974.
[82] R. Schlögl, *Angew. Chem. Int. Ed.* **2015**, *54*, 3465–3520; *Angew. Chem.* **2015**, *127*, 3531–3589.
[83] S. Kuld, C. Conradsen, P. G. Moses, I. Chorkendorff, J. Sehested, *Angew. Chem. Int. Ed.* **2014**, *53*, 5941–5945; *Angew. Chem.* **2014**, *126*, 6051–6055.
[84] J.-D. Grunwaldt, A. M. Molenbroek, N.-Y. Topsøe, H. Topsøe, B. S. Clausen, *J. Catal.* **2000**, *194*, 452–460.
[85] I. Beinik, M. Hellström, T. N. Jensen, P. Broqvist, J. V. Lauritsen, *Nat. Commun.* **2015**, *6*, 1–9.
[86] L. Vegard, *Zeitschrift für Phys. A* **1921**, *5*, 17–26.
[87] H. L. Hong, Q. Wang, C. Dong, P. K. Liaw, *Sci. Rep.* **2014**, *4*, 7065.

[88] V. A. Lubarda, *Mech. Mater.* **2003**, *35*, 53–68.
[89] H. W. King, *J. Mater. Res. Technol.* **1966**, *1*, 79–90.
[90] A. D. Pelton, *Bull. Alloy Phase Diagrams* **1987**, *8*, 42–43.
[91] M. Monte, G. Munuera, D. Costa, J. C. Conesa, A. Martínez-Arias, *Phys. Chem. Chem. Phys.* **2015**, *17*, 29995–30004.
[92] J. Schumann, T. Lunkenbein, A. Tarasov, N. Thomas, R. Schlögl, M. Behrens, *ChemCatChem* **2014**, *6*, 2889–2897.
[93] T. Kandemir, F. Girgsdies, T. C. Hansen, K.-D. Liss, I. Kasatkin, E. L. Kunkes, G. Wowsnick, N. Jacobsen, R. Schlögl, M. Behrens, *Angew. Chem. Int. Ed.* **2013**, *52*, 5166–5170; *Angew. Chem.* **2013**, *125*, 5271–5276.
[94] S. A. McDonald, C. Holzner, E. M. Lauridsen, P. Reischig, A. P. Merkle, P. J. Withers, *Sci. Rep.* **2017**, *7*, 5251.
[95] R. M. German, in *Sinter. Adv. Mater. Fundam. Process.* (Ed.: Z. Z. Fang), Woodhead Publishing Limited, Oxford, **2010**, pp. 3–32.
[96] R. P. Reed, R. E. Schramm, *J. Appl. Phys.* **1974**, *45*, 4705–4711.
[97] P. L. Hansen, J. B. Wagner, S. Helveg, J. R. Rostrup-Nielsen, B. S. Clausen, H. Topsøe, *Science* **2002**, *295*, 2053–2056.
[98] D. A. M. Monti, A. Baiker, *J. Catal.* **1983**, *83*, 323–335.
[99] P. Malet, A. Caballero, *J. Chem. Soc. Faraday Trans. 1* **1988**, *84*, 2369–2375.
[100] G. Held, F. Venturini, D. C. Grinter, P. Ferrer, R. Arrigo, L. Deacon, W. Quevedo Garzon, K. Roy, A. Large, C. Stephens, A. Watts, P. Larkin, M. Hand, H. Wang, L. Pratt, J. J. Mudd, T. Richardson, S. Patel, M. Hillman, S. Scott, *J. Synchrotron Radiat.* **2020**, *27*, 1153–1166.
[101] G. Ashiotis, A. Deschildre, Z. Nawaz, J. P. Wright, D. Karkoulis, F. E. Picca, J. Kieffer, *J. Appl. Crystallogr.* **2015**, *48*, 510–519.
[102] A. Vamvakeros, S. D. M. Jacques, M. di Michiel, V. Middelkoop, C. K. Egan, R. J. Cernik, A. M. Beale, *J. Appl. Crystallogr.* **2015**, *48*, 1943–1955.
[103] A. Vamvakeros, *NDTomo Software Suite*, Github, **2017**.

Manuscript received: March 9, 2022

RESEARCH ARTICLE

Detailed analysis of XRD data reveals insight into the metallic Cu microstructure in industrial-like Cu/ZnO/Al2O3 low temperature water-gas shift (LT-WGS) catalysts as a function of linear and radial distribution in a packed-bed reactor. The presence of Cs in the formulation is revealed to affect the stacking faulting in Cu.

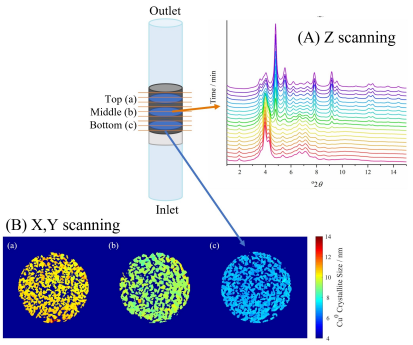

*Dr. D. M. Farmer, Dr. S. D. M. Jacques, Dr. D. Waller, Dr. S. Boullosa Eiras, Dr. K. Roy, Dr. G. Held, Prof. G. Sankar, Prof. A. M. Beale**

1 – 17

Following Cu Microstructure Evolution in $CuZnO/Al_2O_3(-Cs)$ Catalysts During Activation in H_2 using in situ XRD and XRD-CT